Monthly Notices of the ROYAL ASTRONOMICAL SOCIETY

MNRAS **536,** 3803–3815 (2025) https://doi.org/10.1093/mnras/stae2805
Advance Access publication 2024 December 23

Cloud-scale elemental abundance variations and the CO-to-dust-mass conversion factor in M31

Chloe Bosomworth [1,2★] Jan Forbrich [1,2] Charles J. Lada,[2] Nelson Caldwell,[2] Chiaki Kobayashi [1] and Sébastien Viaene[3]

[1]*Centre for Astrophysics Research, University of Hertfordshire, College Lane, Hatfield AL10 9AB, UK*
[2]*Center for Astrophysics | Harvard & Smithsonian, 60 Garden Street, MS 72, Cambridge, MA 02138, USA*
[3]*Sterrenkundig Observatorium, Universiteit Gent, Krijgslaan 281, B-9000 Gent, Belgium*

Accepted 2024 December 15. Received 2024 December 4; in original form 2024 June 11

ABSTRACT

From a spectroscopic survey of candidate H II regions in the Andromeda Galaxy (M31) with MMT/Hectospec, we have identified 294 H II regions using emission line ratios and calculated elemental abundances from strong-line diagnostics (values ranging from subsolar to supersolar) producing both oxygen and nitrogen radial abundance gradients. The oxygen gradient is relatively flat, while the nitrogen gradient is significantly steeper, indicating a higher N/O ratio in M31's inner regions, consistent with recent simulations of galaxy chemical evolution. No strong evidence was found of systematic galaxy-scale trends beyond the radial gradient. After subtracting the radial gradient from abundance values, we find an apparently stochastic and statistically significant scatter of standard deviation 0.06 dex, which exceeds measurement uncertainties. One explanation includes a possible collision with M32 200–800 Myr ago. Using the two-point correlation function of the oxygen abundance, we find that, similar to other spiral galaxies, M31 is well-mixed on sub-kpc scales but less so on larger (kpc) scales, which could be a result of an exponential decrease in mixing speed with spatial scale, and the aforementioned recent merger. Finally, the MMT spectroscopy is complemented by a dust continuum and CO survey of individual giant molecular clouds, conducted with the Submillimeter Array (SMA). By combining the MMT and SMA observations, we obtain a unique direct test of the oxygen abundance dependence of the $\alpha'(^{12}\mathrm{CO})$ factor which is crucial to convert CO emission to dust mass. Our results suggest that within our sample there is no trend of the $\alpha'(^{12}\mathrm{CO})$ with oxygen abundance.

Key words: ISM: HII regions – ISM: abundances – galaxies: individual: M31 – galaxies: ISM.

1 INTRODUCTION

H II regions are clouds of gas that have been photoionized by nearby massive stars, the OB stars, often located near the edges of giant molecular clouds (GMCs). OB stars have a short lifetime of $\lesssim 10$ Myr, therefore the elemental abundances of H II regions can be used to trace recent star formation and thus the latest stages of a galaxy's chemical evolution. Elemental abundance ratios such as oxygen (O) and nitrogen (N) to hydrogen (H) i.e. O/H and N/H (e.g. Pilyugin, Vílchez & Thuan 2010; Sánchez-Menguiano. et al. 2016) as well as N/O (e.g. Belfiore et al. 2017) when traced across an entire galaxy, can be used to investigate its star formation history. Both star formation and the chemical history of galaxies are critical to our understanding of galaxy formation and evolution (Henry & Worthey 1999).

Stars form from the interstellar medium (ISM) and nucleosynthesis gives rise to an increasing abundance of heavier elements (e.g. O and N) which are returned to the ISM upon death of the star. In disc galaxies, the resulting trend is dominantly a linear, radial decline in H II region metallicity because of the higher star formation rates in the inner galaxy (Tinsley 1980). Accretion of external low metallicity gas dilutes these products of nucleosynthesis and thus also affects the composition of the ISM.

Early on, measurements of gas-phase metallicity gradients have helped build analytic models of chemical evolution for galaxies (Matteucci et al. 1989). These gradients have also been compared with chemodynamical simulations of galaxies (e.g. Vincenzo & Kobayashi 2020). This topic has recently been summarized in the review papers Kewley, Nicholls & Sutherland (2019) and Maiolino & Mannucci (2019). Once this radial gradient is removed from the data and only residual metallicity, Δ(O/H), differences remain, the presence of higher order differences within the ISM can be explored (e.g. Ho et al. 2017, 2018, Kreckel et al. 2019, Williams et al. 2022).

More recently, the focus has shifted from galactic-scale trends to local variation driven by mixing of the ISM. For example Kreckel et al. (2020) identify a high level of chemical homogeneity over large (kpc) spatial scales, demonstrating that efficient mixing within the ISM on these scales is a common feature in their sample of spiral galaxies. On smaller scales, local enrichment of the ISM can occur due to nearby star formation (e.g. Ho et al. 2017; Groves et al. 2023). *N*-body/hydrodynamical simulations of disc galaxies by Khoperskov et al. (2023) involving multiple spiral arms, a radial metallicity gradient, and local enhancement in the presence of radial

★ E-mail: cb20acq@herts.ac.uk

migration of gas, predict azimuthal scatter in gas-phase metallicity at a given galactocentric radius (GCR) up to ∼0.05 dex associated with the spiral structure.

O and N abundances are used as proxies to trace gas-phase chemical abundances of H II regions throughout galaxies (e.g. Pilyugin et al. 2010, Pilyugin & Grebel 2016). O, produced by massive stars, has a high relative abundance and therefore produces strong optical emission lines, making it the easiest proxy to measure. In stellar nucleosynthesis, N is produced from the CNO cycle. In the primary process, the seed C is produced in the same production site e.g. massive (4–8 $M_{\odot}$) AGB (asymptotic giant branch) stars and rotating massive stars (see footnote 4 in Kobayashi et al. 2023). In Galactic chemical evolution models (Kobayashi, Karakas & Lugaro 2020 and references therein), N enrichment from AGB stars appears at higher metallicities of the ISM due to their longer time-scales than massive stars (the N enrichment is not secondary but just delayed), after the ISM is enriched by massive stars. In the secondary process, N is produced from the CNO already present in the progenitor star, and thus N yield depends on the metallicity of the star (Clayton 1983; Arnett & Chevalier 1996). The secondary N increases also for metal-rich supernovae (SNe), which also appears at high metallicities of the ISM. Because of the combination of these, the N/O ratio is roughly proportional to the initial metallicity of the star-forming gas (see Vincenzo & Kobayashi 2018). Note that, confusingly, the observed N increase at high metallicity is often called 'secondary N', but is caused by both primary process in AGB stars and the secondary process in massive stars.

The Andromeda Galaxy (M31) is our most nearby large spiral galaxy (∼780 pc; Stanek & Garnavich 1998). It has a prominent, star-forming ring at a GCR of approximately 10 kpc, seen in infrared (e.g. Habing et al. 1984; Gordon et al. 2006) and Hα (e.g. Arp 1964; Devereux et al. 1994) images. The star-forming ring, known as the 'Ring of Fire' (RoF), has been shown to split near the position of M32 (Gordon et al. 2006), displaying a second, fainter ring at ∼ 14 kpc GCR (Haas et al. 1998). In this paper, we report subcloud-scale (∼ 5 pc) metallicity measurements toward individual H II regions in M31. We then performed further analysis with a focus on metallicity differences as a function of spatial separation between H II regions. Using MMT/Hectospec (Fabricant et al. 2005), we have conducted a multi-object spectroscopic survey for hundreds of candidate H II regions in M31. We have used line ratio measurements to both classify sources as H II regions (distinguishing from planetary nebulae) and calculate their metallicities with strong-line diagnostics. A range of metallicities and complex trends have been found in the past for some of the same sources by Sanders et al. (2012, hereafter S12).

The most relevant work to this study, given the identical instrumentation used, is the optical spectroscopic survey of M31 conducted by S12. Also using Hectospec data, they identified planetary nebulae (PNe) and H II regions in M31 and calculated O and N abundances for these sources from emission line ratios. For PNe, the temperature-sensitive auroral line [O III]λ4363 is used to calculate direct O abundances. In H II regions, this line is too weak to be detected, and so various strong-line diagnostics are used. These are indirect methods of measuring chemical abundances derived from the relations between ratios of strong emission lines and directly measured metallicities from observations (e.g. Zaritsky, Kennicutt & Huchra 1994; Pilyugin et al. 2010; Marino et al. 2013) or from photoionization models (e.g. Kewley & Dopita 2002) or even a combined calibration approach (e.g. Pettini & Pagel 2004). S12 utilize five different O abundance diagnostics, metallicities were calculated for sample sizes of 48–192 H II regions depending on frequencies of line detections. Radial abundance gradients calculated by S12 are in agreement with previous works using the same methods but also depend on the strong-line diagnostic used. For all diagnostics used, S12 find significant intrinsic scatter. Using their preferred strong-line method for H II regions (O3N2 from Nagao, Maiolino & Marconi 2006), they found that 33 per cent of neighbouring (within 0.5 kpc) pairs of H II regions vary by > 0.3 dex.

PNe observations can also be used to trace galaxy formation and chemical evolution, and this has been done previously for M31 (e.g. S12; Arnaboldi et al. 2022; Bhattacharya et al. 2022; Kobayashi et al. 2023). Compared to H II regions which reflect recent star formation, PNe abundances reflect the older ISM as they are ionized by red-giant stars at the end of their lifetimes. Temperature-sensitive auroral lines such as [O II]λ4363, [O II]λ7325 and [S III]λ6312 are typically stronger in PNe than H II regions and thus detected more often. From the ratio of strong-lines in the spectra to the corresponding auroral line, electron temperature (T_e) can be measured. This allows for their metallicities to be calculated by 'direct' methods (e.g. Bresolin et al. 2010; Bhattacharya et al. 2022). By calculating direct O and argon abundances for > 200 PNe, Bhattacharya et al. (2022) compared the abundance gradients of PNe in the thin and thick discs of M31 and provided evidence that these are chemically distinct. For the thin disc, a significant negative O abundance gradient was found of similar magnitude to those found for M31 H II regions. In comparison, the thicker disc was found to have a slightly positive radial gradient. One explanation offered was that the thin disc formed following a wet-merger event (a major merger of mass ratio 1:5 occuring ∼2.5–4.5 Gyr ago; Bhattacharya et al. 2019); a collision between two gas-rich galaxies, where metal-poor gas was brought in by the satellite galaxy during the merger, causing a burst of star formation. Simultaneously, the thicker disc was 'radially homogenized' due to this wet-merger event (Bhattacharya et al. 2022).

The star formation rate (SFR) of a galaxy depends on the mass of molecular gas (M_{mol}) available in the ISM, and thus the mass of GMCs is crucial to investigating galaxy evolution. From the mass–metallicity relation (MZR; Lequeux et al. 1979) we know that gas-phase O abundance increases with a galaxy's total stellar mass M_*. Mannucci et al. (2010) studied the relationship between (O/H), M_*, and SFR, which defines the FMR (fundamental metallicity relation). Scaling relations have also been found to display secondary dependencies at $z = 0$, the most relevant for this study is the gas–FMR (Bothwell et al. 2016) where at a fixed M_*, O/H is inversely related to M_{mol}. By studying M_{mol} and metallicities of the same GMCs we can begin to investigate these scaling relations.

The primary constituent of GMCs, H_2, is not observable in emission and therefore M_{mol} is often measured indirectly using the second most abundant emitter: carbon monoxide (CO). To convert this to M_{mol}, the conversion factor between CO luminosity and M_{mol} (α_{CO}) is required. α_{CO} is predicted to depend on metallicity; ultraviolet (UV) radiation destroys molecules depending on the amount of extinction present, thus predicting that the CO/H_2 ratio decreases at lower metallicities where UV can penetrate deeper into the clouds (e.g. Pelupessy & Papadopoulos 2009; Shetty et al. 2011). However, in order to calculate α_{CO} we must assume a value for the gas-to-dust ratio. To avoid this, Forbrich et al. (2020) derived the conversion factor for CO luminosity to dust mass (M_{dust}), $\alpha'(^{12}CO)$, which does not depend on this assumption and can be measured more directly. Viaene et al. (2021) report $\alpha'(CO)$ for ^{12}CO and ^{13}CO towards 20 GMCs in M31, some of which we obtained metallicity values for associated H II regions and therefore we directly investigate the dependence of $\alpha'(CO)$ on metallicity.

This paper is structured as follows: in Section 2, we describe our observations and how these were reduced. In Section 3, we discuss our methodology including emission line flux measurements, extinction correction, source classification, and metallicity/abundance measurements. Our results, including radial metallicity gradients and two-point correlation functions of metallicity are presented in Section 4. We present our summary and conclusions in Section 5.

2 OBSERVATIONS AND DATA REDUCTION

2.1 Source selection

Our targets were primarily selected from a catalogue of candidate H II regions (Azimlu, Marciniak & Barmby 2011), many of which are associated with 1 of the 326 known Giant Molecular Associations (GMAs) in M31 from Kirk et al. (2015), from which the previously mentioned Submillimeter Array (SMA) targets were selected. Some additional sources from a Very Large Array (VLA) survey (Toomey et al. in preparation) were also observed. GMAs for which we have α_{CO} measurements from SMA data (Forbrich et al. 2020; Viaene et al. 2021) were of the highest priority for observation so that the effect of metallicity on GMC properties can be investigated. Selecting our targets in this way increased the probability that we would observe H II regions with measurable emission lines.

2.2 Observations

Observations were performed using the Hectospec spectrometer (Fabricant et al. 2005) at the MMT telescope located in Arizona, USA, using the 270 gpm grating covering the wavelength range ∼3700–9150 Å with a 5 Å resolution. Within this wavelength we have access to multiple strong emission lines; Hα, Hβ, [O II]λ3727, [O III]$\lambda\lambda$(4959, 5007), [N II]$\lambda\lambda$(6548, 6584), and [S II]$\lambda\lambda$(6717, 6731). Observations were taken during two separate observing runs; the first in October 2020 and the second in November and December of 2021. Hectospec has 300 fibres with an on-sky fibre radius of 1.5 arcsec (corresponding to ∼5 pc at the distance of M31), and the entire field is ∼1 deg in diameter. This was ideal for our purposes as we aimed to obtain a large sample size of H II regions. For each pointing, these fibres are allocated as follows: on-sky fibres for sky-subtraction (a total of 35 across all runs) (see Section 2.3), 12–24 pointing fibres (located at the outer edge of the spectrograph), with the rest allocated to science targets.

We have high-quality spectra for 294 H II regions in M31, and ∼300 other sources including 44 PNe. The locations of the H II regions are shown in Fig. 1 and were distinguished from PNe as described in Section 3.3. Our target selection process enabled us to observe the entire disc at the galactocentric radii range $\sim 4-21$ kpc. Unsurprisingly, we see that the majority of H II regions in M31 lie within the inner RoF at ∼10 kpc, or the outer RoF at ∼14 kpc (Haas et al. 1998; Gordon et al. 2006), where the majority of star formation occurs in M31 (Lewis et al. 2015). In Fig. 1, we show the inner RoF as defined by Gordon et al. (2006); a circle of ∼10 kpc radius, offset from the galaxy centre by (5.5 arcmin, 3.0 arcmin).

The majority of our targets were observed multiple times, thus allowing us to confirm measurements from multiple spectra. Also, many Kirk et al. (2015) GMAs have multiple associated H II regions in our source sample. As most H II regions are much larger than 5 pc (e.g. Azimlu et al. 2011 sources have diameters up to ∼190 pc) we primarily observe portions of H II regions. Following Sanders et al. (2012), we assume that any inhomogeneities within individual H II regions are small and random and the region observed is representative of the entire H II region within given uncertainties.

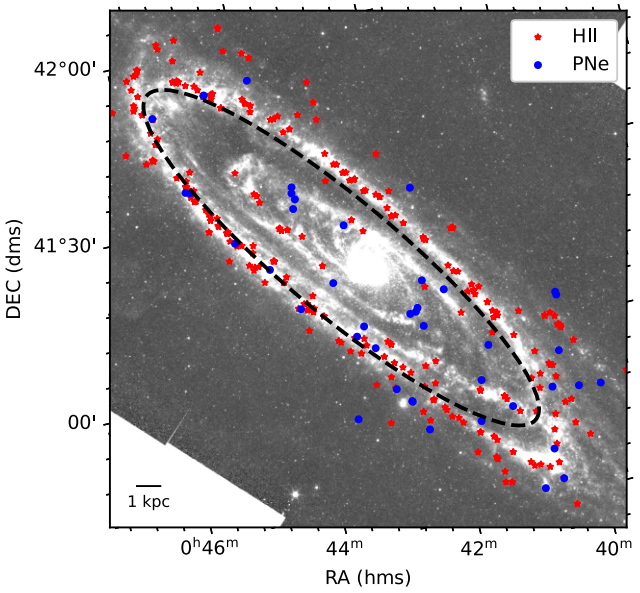

Figure 1. H II regions (stars) and PNe (circles) are shown on the Spitzer MIPS Infrared 24 microns image (Gordon et al. 2006). We display the main RoF as defined by Gordon et al. (2006) as a dashed line. The 1 kpc scalebar represents this distance on-sky at the distance of M31 (780 kpc; Stanek & Garnavich 1998). These are the targets from which we obtained high-quality Hectospec spectra and were able to classify them using their emission line ratios.

2.3 Data reduction

The observations were reduced using the IDL based Hectospec reduction pipeline 'HSRED 2.0' developed by the SAO Telescope Data Center[1], the steps performed are as follows: the frames were first debiased and flat fielded. Separate exposures were compared to identify and remove cosmic rays through interpolation. Individual spectra were then extracted, combined and wavelength calibrated. A number of fibres in each pointing were assigned to blank areas of sky within the focal plane, these are combined and used to perform sky-subtraction on the target spectra. This sky-subtraction method has already been compared to the use of different sky spectra (from areas of the sky ranging from local to distant) in S12 and only small differences were found in emission line ratios (mean difference of ~ 0.01 dex) if different sky spectra were used for data reduction.

We applied a flux correction model to all spectra. There was a lack of known flux-calibration sources in our field of view, therefore, we use calibration information obtained from a 2019 observation of the flux standard Feige 34. This calibration is a per bin correction from 2019 with an identical wavelength axis to our spectra. A typical target airmass of 1.3 was assumed. For matching sources in our and S12 catalogs, we compared our emission line fluxes after flux calibration, but without extinction correction, with their table 2. We found excellent agreement between the emission line fluxes.

[1] https://www.mmto.org/hsred-reduction-pipeline/

Table 1. Emission line flux ratios (relative to Hβ = 100) for M31 H II regions. Nominal uncertainties are estimated from the standard deviation between values obtained from repeat observations of the same source, where available (see the text), with a lower bound of 0.1.

ID	RA, Dec. (J2000)	[O II] λ 3727	[O III] λ 4959	[O III] λ 5007	[N II] λ 6548	Hα λ 6563	[N II] λ 6584	[S II] λ 6717	[S II] λ 6731
1	0:39:13.01, 40:41:44.88	321.6 ± 25.8	26.2 ± 2.1	67.4 ± 5.2	18.5 ± 1.3	291.3 ± 0.6	67.7 ± 3.1	23.7 ± 1.2	18.7 ± 1.1
2	0:39:14.70, 40:48:33.12	459.6 ± 109.0	25.8 ± 3.5	75.0 ± 34.9	20.7 ± 3.5	289.8 ± 1.3	64.5 ± 4.7	31.6 ± 1.5	20.3 ± 1.9
3	0:39:16.50, 40:41:04.92	370.1 ± 7.2	54.3 ± 1.3	159.6 ± 3.2	19.1 ± 1.4	290.3 ± 0.4	56.3 ± 2.9	21.8 ± 1.1	15.9 ± 0.8
4	0:39:55.39, 40:55:49.18	258.0 ± 40.4	13.8 ± 1.0	42.6 ± 1.5	33.0 ± 1.0	293.0 ± 0.2	100.0 ± 2.6	27.4 ± 0.9	19.1 ± 1.1
5	0:40:00.60, 40:39:12.60	357.8 ± 19.3	10.7 ± 2.6	32.0 ± 3.9	40.5 ± 1.5	297.5 ± 1.0	124.6 ± 4.1	26.4 ± 3.9	18.1 ± 1.9
6	0:40:03.89, 40:58:27.12	359.9 ± 48.2	40.9 ± 3.2	126.7 ± 6.6	40.5 ± 1.3	284.9 ± 0.1	119.2 ± 4.3	61.6 ± 0.9	43.3 ± 3.6
7	0:40:04.01, 40:58:53.39	238.9 ± 1.6	41.6 ± 0.1	125.0 ± 1.9	18.9 ± 0.6	284.7 ± 0.1	54.5 ± 2.9	18.8 ± 0.1	13.2 ± 0.3
8	0:40:04.30, 40:58:45.84	407.3 ± 86.9	62.6 ± 0.9	183.6 ± 11.8	38.8 ± 2.9	284.8 ± 0.1	108.9 ± 3.4	49.2 ± 1.7	34.7 ± 0.8
9	0:40:05.30, 40:59:07.44	380.9 ± 89.8	55.7 ± 5.0	164.9 ± 11.3	38.2 ± 1.9	284.8 ± 0.1	100.6 ± 1.4	52.7 ± 1.2	36.4 ± 1.6
10	0:40:06.36, 40:59:04.05	184.9 ± 25.8	71.8 ± 2.1	197.0 ± 5.2	20.9 ± 1.3	284.9 ± 0.6	56.0 ± 3.1	27.4 ± 1.2	18.8 ± 1.1

*Note.*The full table of 294 sources is available online as Supplementary material, we show a portion here for 10 sources.

3 METHODOLOGY AND DATA ANALYSIS

In this section, we describe our methodology. Emission line fluxes were measured with the intention of using the emission line ratios to classify sources, perform extinction correction, and calculate metallicities.

3.1 Emission line fluxes

For emission line flux measurements, we utilize the PYTHON package SPECUTILS (Earl et al. 2024), applying a method similar to that of S12. Due to uncertainty in the flux calibration, we do not compute absolute values for line fluxes. Following S12 and others, we report line fluxes after renormalizing the spectra to Hβ = 100. We extracted line profiles of width 60 Å (centred on the mid-point of the line) and subtract a linear continuum (fit to the two 20 Å ranges on both sides of the line profile). We then fit Gaussians to the continuum-subtracted line profiles for the following lines: Hα, Hβ, [O II]λ3727, [O III]$\lambda\lambda$(4959, 5007), [N II]$\lambda\lambda$(6548, 6584), and [S II]$\lambda\lambda$(6717, 6731), and measure line fluxes. See Appendix A for representative examples. We find line fluxes compatible within uncertainties with those of S12 for any matching sources. In cases where lines are within 60 Å of one another (Hα and [N II]$\lambda\lambda$(6548, 6584) and [S II]$\lambda\lambda$(6717, 6731)), we used a multiple Gaussian fit with one peak centred on each emission line in the range. Continuum subtraction is done still assuming a linear continuum fit, the corresponding extracted spectrum contains the required lines with an extension of 20 Å on both sides.

For each individual target, lines for the same transition were Doppler-shifted due to the blueshift of M31 as a whole and the rotation of the galaxy. We identified an initial velocity guess for each spectrum using the CO velocity field from Nieten et al. (2006) in order to identify the mid-point of each emission line. In the rare case that no CO velocity value is available within 10 pixels of the observation coordinates, the median CO velocity of the entire field, -267 km s^{-1}, was used as an initial guess. This method provided accurate enough wavelength values so that the exact line-mid-points count be determined via a Gaussian fit.

The signal-to-noise (S/N) of the line flux measurements was calculated based on the ratio of the flux value to the rms of the continuum-subtracted noise of 20 Å width on either side of the emission line. We introduced an S/N >5 detection limit for lines so as to ensure we are detecting only emission lines that are clearly above any noise. Extinction-corrected emission line fluxes were used for metallicity calculation after the initial ratio of Hα/Hβ was calculated (see Section 3.2). The extinction-corrected line flux ratios for our final sample of H II regions for which we calculate corresponding abundances (see Section 3.4) are reported in Table 1. We show an example line profile with Gaussian fits for each strong-line measured for one of our spectra in Appendix A. No correction has been made for underlying stellar absorption as we estimate that this will have a very minimal effect on Balmer line fluxes. A test was already conducted on MMT spectra of H II regions in M31 by S12. Models from Starburst99 (Leitherer et al. 1999) were subtracted from underlying continua for both a low and high metallicity H II region. They found that the ratio of Hγ/Hβ changes by 1 per cent at the most from uncorrected values. Additionally, they compared the Hα equivalent widths with extinction (A_v) and found no significant correlation. This indicates that Balmer absorption does not significantly affect measured line ratios for our H II region sample.

While the overall error budget for the emission line flux can be difficult to ascertain, our repeat observations of the same targets provided us with the dispersion of multiple independent measurements for the majority of sources. In the cases in which we have only one observation for a source, the mean percentage uncertainty of this emission line (from sources that do have multiple corresponding spectra) is reported. We introduce a lower bound of 0.1 to uncertainties to reflect unquantifiable systematic uncertainties. We compare these to flux uncertainties derived via error propagation from pipeline-produced sigma spectra, and from those based on line S/N, and found in both cases that these errors were significantly smaller than those from averaging individual runs.

3.2 Extinction correction

Interstellar extinction varies significantly depending on the line of sight and is dependent on wavelength. Dust attenuation affects key observable properties of star formation in galaxies, including emission line fluxes. To account for any discrepancies between emission line fluxes of separate H II regions due to dust attenuation, we applied the optical/near-infrared (NIR) extinction curve from Cardelli, Clayton & Mathis (1989) with $R_v = 3.1$. Since H II regions are primarily ionized by photons of energy 13.6 eV which are usually not reabsorbed, case B recombination is assumed along with electron density and temperature typical of H II regions (10^4cm^{-2} and 10^3K, respectively). An intrinsic Balmer line ratio of Hα/Hβ = 2.86 is expected (Osterbrock & Ferland 2006). We calculated a value for visual extinction (A_V) for each source following the method of Momcheva et al. (2013). Our extinction values were found to be compatible with those of S12 for the 20 sources we have in common.

Table 2. Chemical abundances for M31 H II regions. Nominal uncertainties are estimated from the standard deviation between values obtained from repeat observations of the same source, where available (see the text), with a lower bound of 0.01.

ID	RA, Dec. (J2000)	R[a] (kpc)	Av[b] (mag)	(O/H)∗ R-cal[c]	(O/H)∗ S-cal[d]	(O/H)∗ Z94[e]	(N/H)∗ R-cal[f]
1	0:39:13.01, 40:41:44.88	16.07	1.00 ± 0.13	8.42 ± 0.02	8.50 ± 0.01	8.89 ± 0.03	7.34 ± 0.05
2	0:39:14.70, 40:48:33.12	18.33	0.66 ± 0.15	8.36 ± 0.05	8.47 ± 0.03	8.71 ± 0.18	7.16 ± 0.15
3	0:39:16.50, 40:41:04.92	15.44	0.08 ± 0.04	8.39 ± 0.02	8.47 ± 0.01	8.69 ± 0.01	7.26 ± 0.03
4	0:39:55.39, 40:55:49.18	15.56	0.54 ± 0.01	8.55 ± 0.01	8.61 ± 0.01	9.01 ± 0.05	7.67 ± 0.05
5	0:40:00.60, 40:39:12.60	11.00	0.33 ± 0.08	8.57 ± 0.01	8.67 ± 0.01	8.90 ± 0.03	7.64 ± 0.04
6	0:40:03.89, 40:58:27.12	15.51	0.40 ± 0.15	8.62 ± 0.01	8.58 ± 0.02	8.75 ± 0.05	7.75 ± 0.04
7	0:40:04.01, 40:58:53.40	15.69	1.16 ± 0.01	8.44 ± 0.01	8.49 ± 0.01	8.90 ± 0.01	7.42 ± 0.03
8	0:40:04.30, 40:58:45.84	15.59	0.88 ± 0.08	8.61 ± 0.02	8.58 ± 0.01	8.60 ± 0.12	7.69 ± 0.09
9	0:40:05.30, 40:59:07.44	15.61	0.68 ± 0.14	8.59 ± 0.02	8.55 ± 0.01	8.66 ± 0.11	7.67 ± 0.11
10	0:40:06.36, 40:59:04.05	15.43	0.75 ± 0.13	8.50 ± 0.02	8.45 ± 0.01	8.84 ± 0.03	7.61 ± 0.05

Note.[a] Source galactocentric radius, calculated as described in Section 4. [b] Extinction values calculated as described in Section 3.2. [c] O abundance values calculated using the PG16 R-calibration. [d] O abundance values calculated using the PG16 S-calibration. [e] O abundance values calculated using the Z94 calibration. [f] N abundance values calculated using the PG16 R-calibration. The full table of 294 sources is available online as Supplementary material, we show a portion here for 10 sources. ∗ (O/H) = 12 + log(O/H) and (N/H) = 12 + log(N/H).

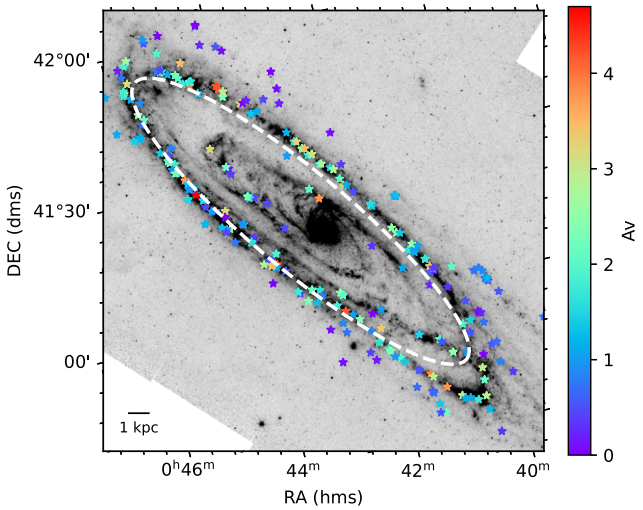

Figure 2. H II regions from our sample overplotted on to the *Spitzer* MIPS Infrared 24 microns image (Gordon et al. 2006), the colourscale for symbols represents values of A_V. As in Fig. 1, we show the RoF fit from Gordon et al. (2006), in this case as a white dashed line. The 1 kpc scalebar represents this distance on-sky at the distance of M31 (780 kpc; Stanek & Garnavich 1998).

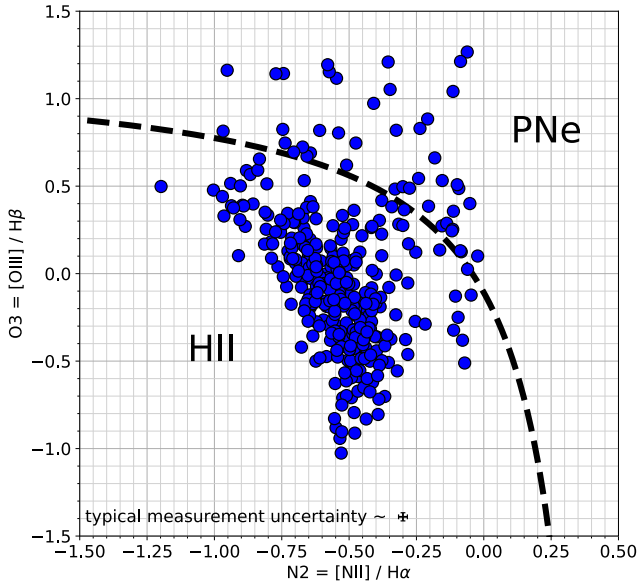

Figure 3. BPT diagram (Baldwin et al. 1981) to distinguish H II regions and PNe from our optical spectra. The classification divider of Kniazev et al. (2008) is shown. The uncertainty is derived from the mean standard deviation of repeated observations of the same sources.

Our A_V values ranged from 0 to 4.7 with a median value of 1.1. Individual A_V for our sample are reported in Table 2.

Fig. 2 displays the H II region positions coloured by their corresponding extinction values. We find that the majority of A_V values lie within the range $0 < A_V < 3$. The background image, the Spitzer MIPS Infrared 24 microns image (Gordon et al. 2006), highlights the dust distribution of M31, as expected the majority of dust is contained within the RoF. The lowest extinction values are mainly located in the outer galaxy, outside of the RoF, showing that our extinction values are consistent with the dust distribution within the galaxy. We note that there is also a range of $A_V \sim 0 - 4.7$ for H II regions within the RoF.

3.3 Classification

Strong emission lines are a characteristic of ionized nebulae, of which H II regions and PNe are two main types. Both display the same emission lines, but can be distinguished from their line ratios using a BPT (Baldwin, Phillips, Terlevich) diagram (Baldwin, Phillips & Terlevich 1981). Line intensity ratios for H II regions and PNe are different due to their primary excitation mechanisms; H II regions have massive OB stars at their centres, whereas PNe have much hotter low/intermediate mass central stars. Though these can also often be distinguished by their optical morphology, classification from emission line ratios allowed us to identify even those very compact H II regions that may be mistaken for PNe. We apply the classification of Kniazev, Pustilnik & Zucker (2008) using the emission line flux ratios [O III]/Hβ (O3) and [N II]/Hα (N2). Positions of our sources on the diagram of O3 versus N2 are shown in Fig. 3. Although we ultimately classified our sources using the Kniazev et al. (2008) classification, multiple classification dividers exist in literature (e.g. Kewley et al. 2001; Kauffmann et al. 2003; Stasińska et al. 2008) indicating that there is an uncertainty in H II region classification

when a source lies close to the defined boundary. Finally, we remove another 15 sources from our H II region sample which have previously been classified as supernova remnants (SNRs) or symbiotic stars. In Fig. 3, the typical uncertainty was calculated from the mean standard deviation between repeat observations in the N2 and O3 emission line ratios.

We note that the number of H II regions that we can classify from our entire data set from the BPT diagram as shown in Fig. 3 is larger than the number of H II regions for which we can calculate O and N abundances (see Section 3.4). The reason for this is that the BPT diagram requires only the lines Hα, Hβ, and the stronger lines of the [O III] and [N II] doublets ([O III]λ5007 and [N II]λ6584), therefore we only require these lines to have S/N $>$ 5. By implementing a minimum S/N for these four lines only, we obtain 416 H II regions. In Fig. 3, we include only those sources which have a S/N $>$ 5 for all lines required to calculate abundances as described in Section 3.4. Therefore, we include 309 H II regions (15 of which are removed from the final sample, as previously mentioned, due to being previously classified as SNR or symbiotic stars) and 44 PNe.

3.4 Strong-line diagnostics

The use of strong-line diagnostics for our metallicity calculations allows us to probe a sample of H II regions covering the entire galactic disc. In comparison, we have access to the temperature-sensitive auroral line, [O III]λ4363, for just four H II regions. Various methods for calculating gas-phase metallicities and abundances (mainly O and N) from strong emission lines exist in literature, derived for various different combinations of emission line ratios. Calibrations can be either empirical or theoretical (see section 4 of Kewley & Ellison 2008 for a full review of the topic). Empirical calibrations are derived from the relationship between T_e-based abundances and strong-line ratios (e.g. Pettini & Pagel 2004), whereas theoretical calibrations are derived from the relationship between strong-line ratios and a photoionization model (sometimes combined with T_e-based abundances e.g. Kewley & Dopita 2002; Kobulnicky & Kewley 2004). Metallicity values are then often plotted with respect to their galactocentric radii so that a radial gradient can be calculated. S12 applied five different diagnostics for O abundance to their sample of H II regions in M31: Zaritsky et al. (1994), Kewley & Dopita (2002), Pilyugin & Thuan (2005), and two from Nagao et al. (2006) utilizing different calibrating emission line ratios. Their results show that the diagnostic chosen affects the metallicity values calculated, along with the metallicity gradient. The uncertainty in absolute metallicity (O) values can vary up to 0.6 dex depending on the strong-line diagnostic used (Kewley & Ellison 2008).

It is for these reasons that we carefully consider our choice of strong-line diagnostic. In recent works, the strong-line abundance diagnostics of Pilyugin & Grebel (2016, hereafter PG16) are increasingly popular for the purpose of calculating metallicities of individual H II regions (e.g. Kreckel et al. 2019, 2020; Williams et al. 2022) due to the strong agreement (within $\sim$ 0.1 dex) with direct, T_e based O abundances (see Ho 2019). We also note that since we are observing fractions of H II regions within the beam size, we are sensitive to internal ionization parameter fluctuations of H II regions (Jin et al. 2023). The calibration of PG16 provides us with two diagnostics for O abundance (R- and S-calibration) and one N abundance diagnostic (R-calibration). The following emission line ratios are utilized in the PG16 calibrations:

$$N_2 = ([N\,II]\lambda6548 + [N\,II]\lambda6584)/H\beta$$
$$R_2 = (O\,II]\lambda3727 + [O\,II]\lambda3729)/H\beta$$
$$R_3 = ([O\,III]\lambda4959 + [O\,III]\lambda5007)/H\beta$$
$$S_2 = [S\,II]\lambda6717 + [S\,II]\lambda6731/H\beta.$$

The spatial resolution of our data is not sufficient to resolve the [O II] doublet and so these lines are blended in our data. We obtain a single line flux for [O II] from a line of rest wavelength 3727 Å which is a sum of both lines. The R-calibration utilizes the line ratios N_2, R_2, and R_3 whereas the S-calibration utilizes the ratios N_2, S_2, and R_3, making these calibrations three-dimensional (3D). The high dimensionality of these diagnostics make it less sensitive to ionization parameter than 1D and 2D diagnostics. We calculate both O and N abundance values using the PG16 method, using nitrogen as our secondary tracer to further confirm any trends. Many strong-line diagnostics, including PG16, separate H II regions into upper (high-metallicity) and lower (low-metallicity) branches and calibrate these separately, distinguished by the N_2 line ratio. All of our H II regions lie on the upper-branch.

As previously discussed, the diagnostic chosen affects the metallicity values calculated. S12 have already compared four different O abundance diagnostics to their sample of H II regions in M31. In order to directly compare metallicities calculated for any matching sources in our sample, we apply the O abundance diagnostic of Zaritsky et al. (1994, hereafter Z94) also used in S12. Z94 is another empirical calibration, based on the strong-line ratio R_{23} = ([O III]λ3727 + [O III]$\lambda\lambda$(4959, 5007))/Hβ (Pagel et al. 1979). The Z94 method was chosen because it was derived from a similar data set to ours; observations of individual H II regions in spiral galaxies, including MMT observations. It is only calibrated for high-metallicity (12 + log(O/H) $>$ 8.4 dex) H II regions, which includes almost our entire sample if metallicities are calculated via the Z94 method. For the same H II regions that are present in both our and the S12 samples, we find that Z94-calculated metallicities are in agreement within their respective uncertainties. The Z94 diagnostic is more sensitive to ionization parameter fluctuations than the PG16 diagnostics as it only depends on one emission line ratio, and thus we use the PG16-derived metallicities in future discussion. O and N abundance values calculated using different calibrations for individual H II regions in our sample are reported in Table 2.

We estimate uncertainties in abundances for each diagnostic measured, again using the standard deviation of repeat observations of the same source, reflecting the total empirical error budget. Where a source has just one corresponding observation, the quoted uncertainty in Table 2 is the mean percentage uncertainty calculated for sources for which we have multiple observations. Additionally, we introduce a lower bound of 0.01 to uncertainties, again to reflect unquantifiable systematic uncertainties. The standard deviation probes the overall error budget accounting for differences in atmospheric conditions between observations and slight differences between the individual Hectospec optical fibres. Uncertainties in absolute abundance due to the chosen metallicity diagnostic may be as large as 0.7 dex (Kewley & Ellison 2008) (although empirical calibrations produce O abundances that are in better agreement with directly measured abundances), however, we are interested in metallicity differences between individual H II regions more than the absolute metallicity values. Work analysing the reliability of relative H II region O abundances have shown that these are statistically robust between different calibrations (e.g. Ho et al. 2017). Finally, we note that selection effects may occur due to emission line detection; any

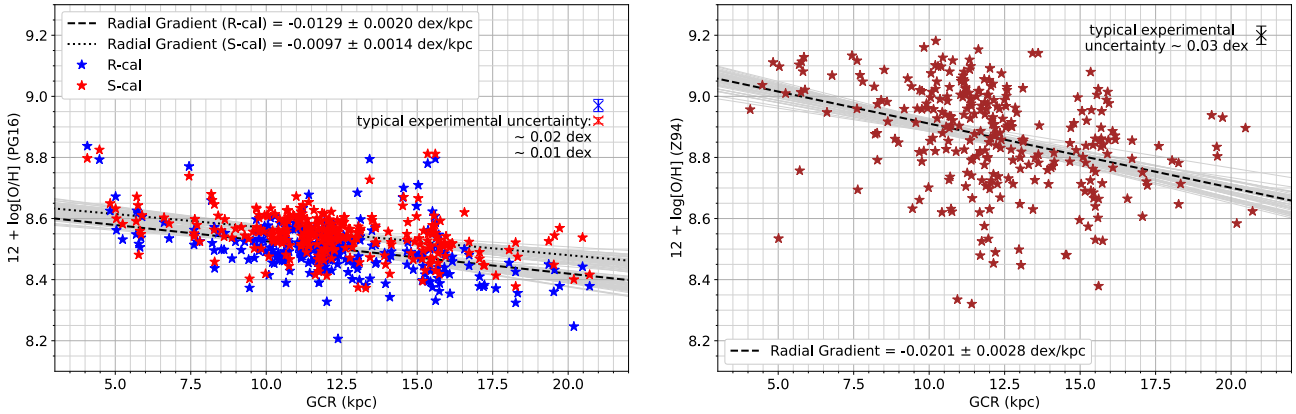

Figure 4. O abundance (12 + log[O/H]) for H II regions in M31 from the *left*: PG16 R and S-calibrations *right*: Z94 diagnostics as a function of galactocentric radius (GCR kpc).

spectra without all of the required lines detected at sufficient S/N could not be included in analysis. However, since we are analysing strong emission lines, this likely has little affect on resulting trends.

4 RESULTS AND DISCUSSION

We derived the radial O and N abundance gradients across M31 for H II regions using strong-line methods Z94 and PG16 as outlined in Section 3.4. The galactocentric radius (GCR) of each H II region was calculated following Haud (1981). We assume the galactic centre of M31 and its position angle (PA) to be:

$\alpha_0 = 00^\circ42'44\farcs52$ (J2000)

$\delta_0 = +41^\circ16'08\farcs69$ (J2000)

$\Theta_0 = 37^\circ42'54''$

(Haud 1981) and the angle of inclination to be $i = 12.5^\circ$ (Simien, Pellet & Monnet 1979). We note that these deprojected distances from the galactic centre of M31 rely on the assumption that all positions are within the same plane, and so some separations may be underestimated.

The following sections are structured as follows. First, we present results for radial O and N abundance gradients in M31. Then, we subtract the radial trend from our data in order to analyse reduced and enhanced abundances (compared to the radial average) and search for azimuthal trends around the RoF or variation with spiral arm structure. We look at the two-point correlation function of metallicity with source separation scale and compare to other galaxies from Kreckel et al. (2020) and Williams et al. (2022). Finally, we analyse the relationship between H II region metallicities and the conversion factor for ^{12}CO luminosity to dust mass (M_{dust}), $\alpha'(^{12}CO)$.

4.1 Radial abundance gradients

Fig. 4 shows H II region metallicities as a function of R. We show the typical uncertainty of a given measurement as the mean standard deviation between repeat observations of the same sources. We then calculated the radial metallicity (O abundance) gradients for our sample of 294 H II regions from each calibrations, calculated from bootstrap resampling of least-squares fitting. Gradient uncertainties correspond to the standard deviation of the individual bootstrap gradient calculations.

For the PG16 calibrations we find radial gradients of -0.0129 ± 0.0020 dex kpc^{-1} (R-calibration) and -0.0097 ± 0.0014 dex kpc^{-1} (S-calibration), which are in agreement within 2σ. Both values are in agreement within 1σ with values that S12 obtained using the diagnostics of Kewley & Dopita (2002) and Nagao et al. (2006). The S-calibration result is also consistent with the S12 result using the Pilyugin & Thuan (2005) diagnostic within 1σ. Thus, despite improving on individual metallicity uncertainties due to ionization parameter fluctuation, the radial metallicity gradient derived from PG16-derived metallicities is still somewhat dependent on the calibration method. Separating the galaxy into two halves down the minor axis, we calculated radial gradients for the two halves of the galaxy, obtaining -0.0103 ± 0.0022 dex kpc^{-1} for PA < 180 deg and -0.0066 ± 0.0024 dex kpc^{-1} for PA > 180 deg. The values are both consistent with the radial gradient of the full sample and with one another within 1σ uncertainties.

The metallicity (O abundance) gradient we calculate from the Z94 diagnostic as shown in Fig. 4 (right) is -0.0201 ± 0.0028 dex kpc^{-1}. This result is in agreement within 1σ with the radial metallicity gradient calculated by Sanders et al. (2012) also using Z94-derived abundances (-0.0208 ± 0.0048 dex kpc^{-1}) and that calculated by Z94 (-0.020 ± 0.007 dex kpc^{-1}). The radial metallicity gradients in our work calculated from the Z94 and the PG16 R-calibration agree within 2σ (Z94 and PG16 S-calibration agree within 3σ). Therefore the radial metallicity gradient of M31 is again dependent on which strong-line diagnostic is chosen to calculate individual H II region metallicities.

Wenger et al. (2019) built on previous Milky Way (MW) H II region studies (e.g. Balser et al. 2011) finding an O abundance gradient of -0.052 ± 0.004 dex kpc^{-1} from T_e line measurements. A radial O abundance gradient of -0.041 ± 0.006 dex kpc^{-1} was calculated by Esteban & García-Rojas (2018). Compared to the O abundance gradients calculated in this work from PG16 diagnostics (which has agreement within ∼0.1 dex with direct, T_e-based metallicity measurements; Ho 2019), the radial gradient of the MW is ∼ 4–6 times steeper than that of M31. Kreckel et al. (2019) found O abundance gradient values for their sample of eight spiral galaxies, also derived from PG16 S-calibration abundances, ranging from -0.0199 to -0.1586 dex kpc^{-1} (excluding one galaxy which produced a positive gradient). Therefore, the O abundance gradient of M31 is shallow compared to these spiral galaxies.

Again from bootstrap resampling, we calculate an N abundance gradient of -0.0334 ± 0.0038 dex kpc^{-1} from 294 H II regions using the R-calibration of PG16. We display this result in Fig. 5. The

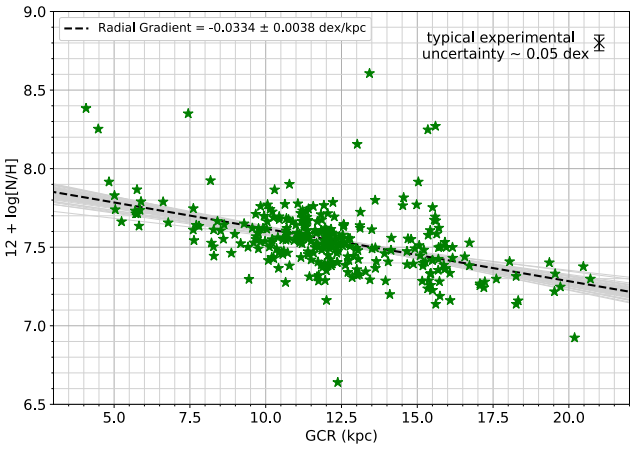

Figure 5. N abundance (12 + log[N/H]) for H II regions in M31 from the PG16 R-calibration as a function of galactocentric radius (GCR kpc).

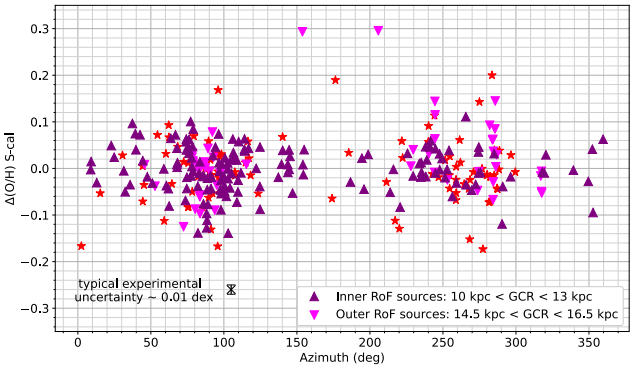

Figure 6. O abundance (12 + log[O/H]) for H II regions in M31 from the PG16 S-calibration as a function of azimuthal angle with 0° corresponding to the minor axis in the northern direction and moving in the clockwise direction. Sources which are located within the main RoF component at ~10–13 kpc are shown by triangles. Sources located within the outer RoF component at ~14.5–16.5 kpc are shown by inverted triangles.

N abundance gradient is significantly larger than the O abundance gradient by a factor of ~1.7–3.4 depending on the choice of strong-line diagnostic. This is consistent with simulations from Vincenzo & Kobayashi (2018) where they find increasing N/O with O/H in spatially resolved star-forming disc galaxies, and a resulting negative radial N/O abundance gradient.

The N abundance gradient calculated in this work is compatible with that from S12 (-0.0303 ± 0.0049 dex kpc^{-1}) which uses the strong line diagnostic of Pilyugin et al. (2010), an older version of the N abundance diagnostic from PG16. For the MW, Esteban & García-Rojas (2018) found N abundance gradients ranging between -0.047 to -0.050 ± 0.008 dex kpc^{-1} from direct H II region abundances of 13 sources. This is steeper than the N abundance gradient found in this work for M31 by a factor of ~1.4–1.5. As found for the O abundance gradient, there is statistically significant scatter around the N abundance gradient, thus providing further evidence that there is abundance variation beyond the radial gradient. Figs 4 and 5 show that H II regions at a similar GCR can have very different metallicities, as also shown in S12 in their figs 8 and 14.

Although our abundance gradients are in agreement with previous work, Figs 4 and 5 show that there is significant (greater than the typical uncertainty) scatter around the radial gradient at all galactocentric radii. The majority of M31 H II regions are located at ~12 and 15 kpc. These correspond to the approximate locations of the main RoF and its outer component at (Lewis et al. 2015). If the metallicity variation throughout M31 could be fully explained by just the radial gradient, we would expect that these sources all have a similar metallicity. However, in Fig. 4 (left), we see O abundances ranging from ~8.35 to 8.75 dex (excluding two outliers), from PG16 S-calibration-based abundances, for sources within the RoF (~10–16 kpc). The metallicity range covered by RoF H II regions is even larger for the Z94 diagnostic (~8.4–9.2 dex) though this is partially due to the inherent noise of the diagnostic. S12 found no dependence of metallicity or gradient on the surface brightness of H II regions for their similar sample.

Our final H II region sample requires all emission lines required for the strong line calibrations (see Section 3.4) to have S/N > 5, producing a sample size of 294. We can, theoretically, extend our sample size by assuming a 3:1 ratio for the strong to weak lines in the [O III] and [N II] doublets (Storey & Zeippen 2000). We investigated this following the method outlined in Kreckel et al. (2020): we measure only the lines [O III]λ5007 and [N II]λ6584, the stronger lines in each doublet, and divide these line fluxes by 3 to obtain the line fluxes of [O III]λ4859 and [N II]λ6548. Therefore, the condition that the weaker lines of the doublet must have S/N > 5 for the abundances to be recorded can be eliminated, increasing the number of H II regions to 322. This is lower than the 416 classified H II regions (see Section 3.3) because both of the lines in the [S II] doublet are still required to have S/N > 5. Calculating the radial metallicity gradients for the extended sample, we obtain values compatible within 1σ to the previously reported values in this section, for all abundance diagnostics and tracers. Ultimately, the 3:1 ratio assumption does not significantly increase our sample size and leads to no change to our results. Therefore, we use our sample of 294 H II regions, measuring both lines in the [O III] and [N II] doublets, for all further analysis.

4.2 Non-radial trends

We next subtract the S-calibration radial-gradient from individual H II region O abundance values, so that only residual metallicity remains. We chose to use the S-calibration abundance values for this purpose because the [S II] lines are less affected by extinction than the [O II] line (see fig. 3 from Cardelli et al. 1989), decreasing the inherent uncertainty. This is also identical to the calibration used in other works investigating H II region metallicity scatter across galaxy discs (e.g. Kreckel et al. 2019) enabling us to make a direct comparison without the uncertainty due to using different calibrations. This enables us to investigate any second-order trends such as azimuthal effects and variations corresponding to galactic features such as spiral arms and the RoF. In Fig. 6, we show Δ(O/H) of H II regions as a function of azimuthal position in the galaxy for the PG16 S-calibration. From this plot we find little evidence of systematic metallicity trends in the azimuthal direction, but that scatter of standard deviation 0.06 dex around the radial gradient occurs across the entire galaxy. This is true even for sources at a similar R, as shown for the sources located within the RoF at ~10–13 kpc as well as its outer component at ~14.5–16.5 kpc, highlighted on Fig. 6.

Previous studies have shown that significant scatter around the radial gradient typically occurs distributed across the galaxy (Kreckel et al. 2019; Grasha et al. 2022). Alongside this, studies have shown hints of distinct azimuthal variation in the form of enhanced abundances along spiral arms (e.g. Kreckel et al. 2019; Grasha et al. 2022), although statistical tests failed to quantify a systematic

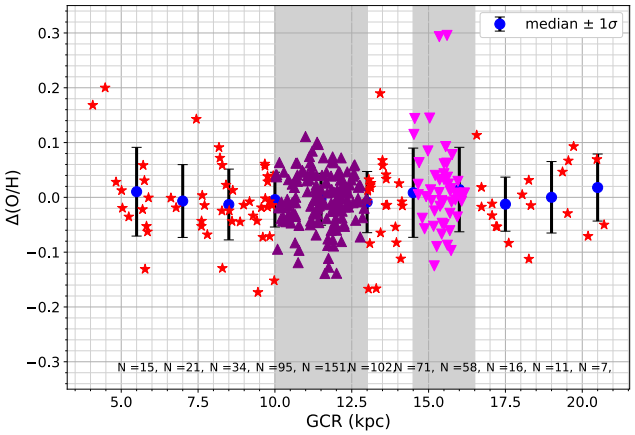

Figure 7. Variation of Δ(O/H) (PG16 S-calibration) with GCR, for individual H II regions (stars) and the mean values for bins of equal radial size (3 kpc) shown as circles. Bins are separated by 1.5 kpc and overlap by 50 per cent. Sources located within the main RoF at ∼10–13 kpc are shown by triangles and sources located within the outer RoF component at ∼14.5–16.5 kpc are shown by inverted triangles. In the shaded regions, we show the approximate positions and widths of the RoF components, based on where the majority of our sources lie. In this case, the black bars show the standard deviation dispersion of the sources in each bin, which have *N* number of sources.

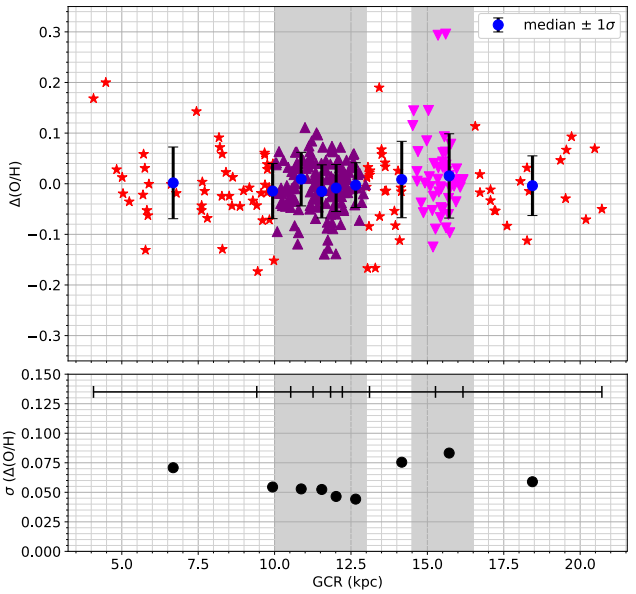

Figure 8. *Top*: the same as Fig. 7 but for bins of approx. equal number of sources ($N = 34$ or 35). Sources located within the RoF at ∼10–13 kpc are shown by triangles and sources located within the outer RoF component at ∼14.5–16.5 kpc are shown by inverted triangles. The shaded regions represent approximate RoF positions, the same as for Fig. 7. Solid bars give the standard deviation of sources in each bin. *Bottom*: Standard deviation with varying GCR. The bars show the radial range covered by each bin, relevant to both figures.

correlation due to the large scatter present across the entire galaxy. On the other hand, Ho et al. (2017) found a statistical difference between spiral-arm and inter-arm regions, finding that 76 per cent of H II regions within the main spiral are above the radial gradient whilst only 19 per cent of inter-arm regions are above the gradient. We note that in these spiral galaxies, the majority of H II regions are located within the spiral arms, however, in M31 the majority are located in the RoF. For H II regions located in the RoF, we see an approx. equal number of reduced abundance H II regions as we do enhanced abundance H II regions. This could suggest that we are seeing the effect of a recent collision with M32 adding some more pristine gas that would otherwise not be present, predicted to have occured ∼200–800 Myr ago (Block et al. 2006; Davidge et al. 2012; Dierickx, Blecha & Loeb 2014).

A strong positive correlation between Δ(O/H) and ionization parameter hints that local enrichment is linked to differences in the local physical conditions (Grasha et al. 2022). Along with evidence that H II regions with enhanced abundances have high-ionization parameter, Hα luminosity, younger star clusters, and high CO in the associated molecular clouds (Kreckel et al. 2019), this suggests that local enrichment has occurred due to recent star formation. Kreckel et al. (2019) see correlation between reduced abundance H II regions and an increased Hα velocity dispersion which indicates the dynamical state of the ionized gas. This indicates that large-scale mixing may have taken place, introducing pristine material from outside the galaxy.

We suggest that a similar explanation may be relevant to M31. In Figs 7 and 8, we show the mean and standard deviation Δ(O/H) at varying bins of GCR. Fig. 7 uses bins of equal radial widths (3 kpc) that overlap by 50 per cent of the bin size. For Fig. 8, we use bins containing approximately equal numbers of sources, where N = 34 or 35. In both figures, we see that the standard deviation in the scatter of Δ(O/H) is of the range ∼0.03–0.10 dex and that approx. ∼30 per cent of H II regions have$|\Delta(O/H)| > 1\sigma$ and 20 per cent of those outliers have $|\Delta(O/H)| > 2\sigma$. Approximately 50 per cent of outliers are enhanced abundances (and approximately 50 per cent are reduced abundances) compared to the metallicity gradient. The greatest amount of scatter occurs at GCR ∼ 15 kpc which corresponds with the outer RoF (the corresponding sources are shown as pink upside-down triangles), this is also where we see the most enhanced abundance H II regions. In comparison, the main RoF at ∼10–13 kpc is where we see the least scatter, suggesting that this material is more well-mixed than in the outer RoF component. However, as we see both enhanced and reduced abundances of $|\Delta(O/H)| > 1\sigma$ distributed across the entire disc, general systematic trends have not been identified. We note that we make no statement on the exact location and size of the RoF, and our approximation is based on the distribution of our H II region sample.

The presence of enhanced abundance H II regions indicates that material has likely been enriched due to recent star formation and SNe. Simulations indicate that kpc-scale mixing can take 100–350 Myr (Roy & Kunth 1995; de Avillez & Low 2002). Simulations performed by Avillez & Low (2002) indicate a mixing time-scale of 350 Myr for the Galactic SN rate, therefore it is possible that there is SN-enriched material in M31, primarily within the RoF, that is not yet fully mixed, causing inhomogenities in the ISM to remain.

A possible explanation for the pristine gas is that it may have been brought into M31 from outside of the galaxy, resulting in reduced abundance H II regions. A possible source of this pristine gas is a recent collision with M32 which models predict occurred ∼200–800 Myr ago. Lower-metallicity (in comparison to the metallicity of gas in M31) gas may have been stripped from M32 and not yet fully mixed into M31, especially if the collision occurred closer to ∼200 Myr ago. Most 1σ outliers are located within the RoF, which is believed to have formed during the collision with M32 (Braun 1991). The differences in the standard deviation of the residual scatter are

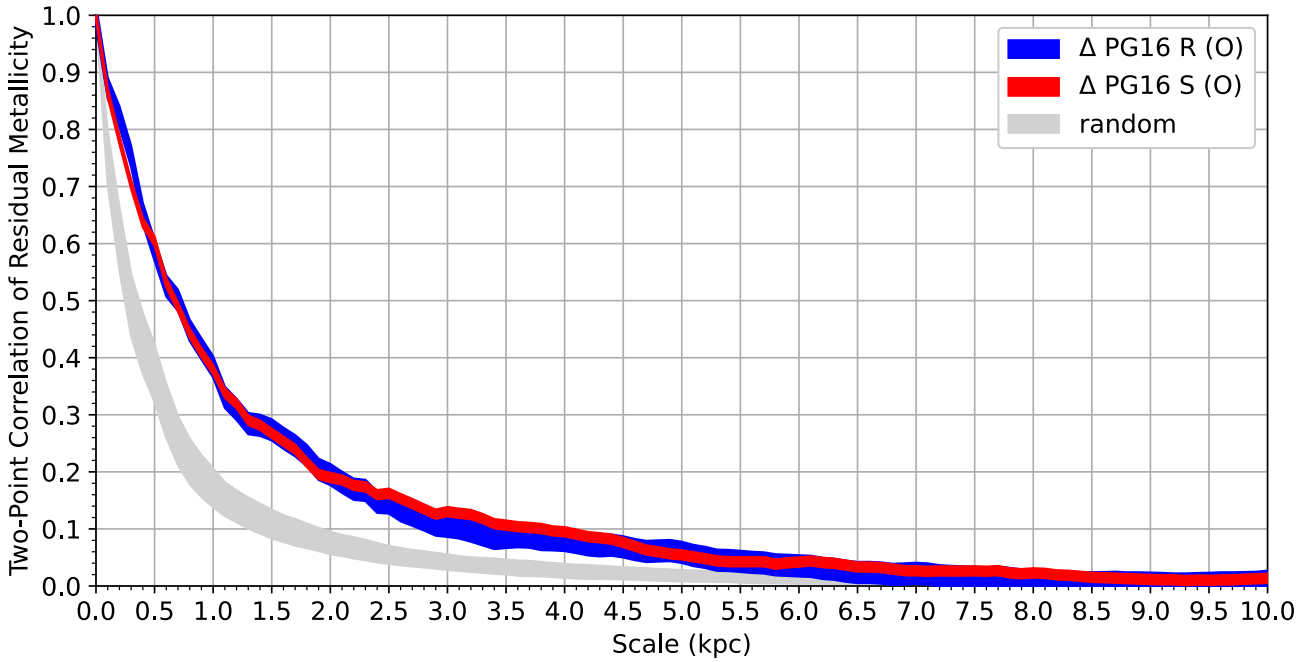

Figure 9. Two-point correlation of metallicity for the PG16 strong-line diagnostics as a function of spatial scale (H II regions separated by up to 10 kpc). For comparison, we show the two-point correlation if the metallicity values are randomized i.e. metallicity and position within the galaxy are uncorrelated.

also displayed in Fig. 8. The global scatter over all values of GCR is ~ 0.06 dex. However, we see in Fig. 8 that the standard deviation can be as low as <0.04 dex within the main/inner RoF, suggesting that this material is well mixed. On the contrary, the standard deviation scatter is as high as >0.09 dex for the outer RoF. In Figs 7 and 8, we see increased scatter in Δ(O/H) at GCR $\sim$ 15 kpc, suggesting that the material in the outer RoF is less well-mixed than the inner RoF. For comparison, Kreckel et al. (2019) found global scatter of 0.03–0.05 dex for their galaxies.

4.3 Two-point correlation function of metallicity

Following the method of Kreckel et al. (2020), we calculate the two-point correlation function of residual metallicity as a function of H II region separation after the radial trend has been subtracted (Fig. 9) using their equation 5. As was also done in their work, we computed a randomized sample by randomly shuffling the metallicity values amongst our H II region positions. For our purpose, we used metallicity (O) values from the PG16 S-calibration. Then we calculate the correlation function via bootstrap resampling and taking the average and standard deviation over 100 iterations. From this we investigate the separation between H II regions where we no longer see the same degree of homogeneity above that expected from the randomized sample.

Our two-point correlation function is shown in Fig. 9. We show that the correlation falls below 0.5 (the 50 per cent correlation scale) at $\sim$ 0.6 kpc separation and below 0.3 at $\sim$ 1.2 kpc separation. This is significantly different to the randomized sample for which the correlation falls below 0.5 at $\sim$ 0.3 kpc separation and below 0.3 at $\sim$ 0.6 kpc separation. From this, we conclude that there is correlation in H II region metallicities for nearby sources above what we would see if the scatter around the radial gradient was completely random. The two-point correlation functions for 19 spiral galaxies are reported in Williams et al. (2022), for which 50 per cent correlation scale values found mostly range from 0.19 to 1.08 kpc apart from for one galaxy which reaches 0.5 correlation at 4.12 kpc. This suggests that M31 is quite well-correlated on small scales which is similar in general to these galaxies, when comparisons are made using the same strong-line diagnostic (PG16 S-calibration). Models of Avillez & Low (2002) predict that mixing slows down exponentially with separation, which is a possible explanation as to why galaxies are typically found to be less well-mixed on kpc scales than on sub-kpc scales.

4.4 Metallicity dependence of $\alpha'(^{12}\mathrm{CO})$

Many of our optical spectra supplement SMA observations for which we have dust continuum emission measurements for individual GMCs (see Viaene et al. 2021). This gives us the opportunity to directly study any apparent metallicity dependence of $\alpha'(^{12}\mathrm{CO})$; the ratio of dust mass and CO luminosity. Both the dust mass and the CO luminosity are likely to vary with metallicity, which could either exacerbate or mitigate ensuing changes of the ratio. What we compare here are Viaene et al. (2021) $\alpha'(^{12}\mathrm{CO})$ measurements for individual clouds and the metallicities for associated H II regions obtained in this study. We plot the resulting relationship between H II region O abundances (from the S-calibration of PG16) and GMC $\alpha'(^{12}\mathrm{CO})$ (as defined in Viaene et al. 2021) in Fig. 10. Despite the statistically significant difference of the metallicity values, we essentially find a constant $\alpha'(^{12}\mathrm{CO})$ of $\sim (0.0605 \pm 0.009)\,\mathrm{M}_{\odot}(\mathrm{K\ km\ s^{-1}pc^{2}})^{-1}$ across the metallicity range probed, apart from the two outliers with large uncertainties. Therefore, there is no evidence for a strong metallicity dependence of $\alpha'(^{12}\mathrm{CO})$ in this work. This finding may be explained by the prediction from Bolatto, Wolfire & Leroy (2013) that a significant change in α(CO) is generally only expected for low metallicities i.e. $12 + \log(\mathrm{O/H}) < 8.4$ dex. We see a hint of this trend in Fig. 10, due to the presence of an outlier metallicity at $\sim$ 8.42 which has higher $\alpha'(^{12}\mathrm{CO})$ than other sources with more than 1σ difference. However, this alone is not enough to make a conclusion on a trend of $\alpha'(^{12}\mathrm{CO})$ with metallicity for our sample, a

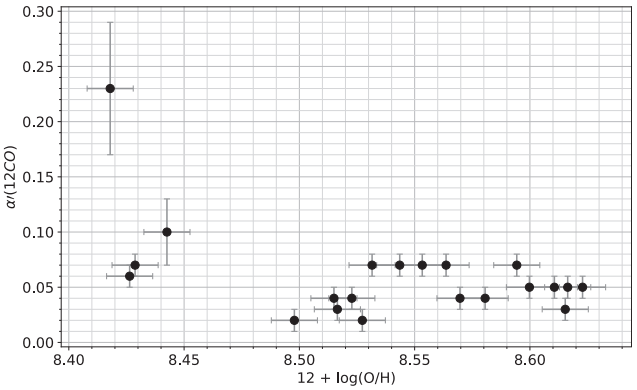

Figure 10. The variation of the CO-to-dust-mass conversion factor, $\alpha'(^{12}\mathrm{CO})$, with metallicity (O) for H II regions with SMA detections reported by Viaene et al. (2021). Some GMCs have multiple associated H II regions. Uncertainties in the S-calibration-calculated metallicities are the same as for Fig. 4. $\alpha'(^{12}\mathrm{CO})$ values and uncertainties are taken from Viaene et al. (2021).

larger sample size spanning the metallicity range 12 + log(O/H) < 8.5 dex is needed to further this particular study. At higher metallicities, this could mean that any impact of metallicity changes in H II region O abundances and GMC $\alpha'(^{12}\mathrm{CO})$ values largely cancels out. However, we note again that $\alpha'(^{12}\mathrm{CO})$ does not take into account the gas-to-dust ratio, which is also predicted to depend on metallicity.

5 SUMMARY AND CONCLUSIONS

From our optical spectroscopic survey of M31 we have identified and calculated O and N abundance values for 294 H II regions from their emission line ratios. From our analysis, we conclude the following:

(i) We find an O abundance gradient of -0.0113 ± 0.0016 dex kpc^{-1} by taking the mean of the gradients calculated using the PG16 R-calibration and S-calibration. We explored the use of the R_{23} diagnostic of Z94, finding that the value of the radial metallicity gradient depends on the chosen calibration (as has been shown in previous studies e.g. S12), but these generally agree within 2σ. Weak auroral lines are necessary to calculate a more precise, direct value, but these are only detected in four of our sources with S/N > 3.

(ii) M31 has a relatively shallow O abundance gradient compared to other spiral galaxies e.g. those from Kreckel et al. (2019). In comparison to the Milky Way it is shallower by a factor of ∼4–6 depending on the choice of methodology.

(iii) We find a N abundance gradient of -0.0334 ± 0.0038 dex kpc^{-1} from the PG16 R-calibration, in agreement within uncertainty with that from S12 calculated for M31 using the diagnostic from Pilyugin et al. (2010).

(iv) The N abundance gradient of M31 is ∼1.7–3.4 (depending on the chosen calibration) times steeper than the O abundance gradient, this indicates that the N/O ratio is higher towards the centre of the galaxy. This is consistent with cosmological simulations (Vincenzo & Kobayashi 2018) which show a negative N/O radial gradient.

(v) Around our S-calibration O radial gradient we measure a standard deviation in scatter of ∼0.06 dex, exceeding the mean inherent measurement uncertainty of ∼0.01 dex. After subtracting the radial gradient from metallicities to get a residual metallicity, Δ(O/H), we see significant outliers that exceed this scatter up to 5σ. This confirms conclusions from previous works (e.g. S12; Kreckel et al. 2020) that a radial gradient is not sufficient to describe metallicity variation between H II regions in spiral galaxies.

(vi) The presence of reduced-metallicity (compared to the radial gradient) H II regions throughout the disc is possible evidence that external gas of lower relative metallicity has been brought into the galaxy, possibly from outside. This may have occurred during a collision between M31 and M32 occurring 200–800 Myr ago. We also see the additional presence of enhanced-metallicity (compared to the radial gradient) H II regions throughout the disc, which previous work suggests is due to ISM enrichment by recent star formation and SNe (Ho et al. 2017).

(vii) From the two-point correlation function, we see that metallicities are well-correlated (compared to the random sample) at subkpc scales. There is evidence of an exponential decrease in the speed of mixing (e.g. Avillez & Low 2002) and so it is expected that kpc-scale inhomogenities will be present for longer periods of time. Additionally, inefficient mixing on larger scales could suggest that not all material brought in by the collision is mixed yet and causes reduced abundance H II regions in our sample.

(viii) We study the variation in $\alpha'(^{12}\mathrm{CO})$ from an SMA survey of the associated GMCs (Viaene et al. 2021) with O abundance. Despite a relatively large range in metallicity, we find no evidence for a significant dependence of $\alpha'(^{12}\mathrm{CO})$ on O abundance at 12 + log(O/H) > 8.42 for H II regions associated with GMCs observed by the SMA. The data point in Fig. 10 with metallicity ∼ 8.42 has a respectively large error bar in comparison to other sources, suggesting that this high $\alpha'(^{12}\mathrm{CO})$ value is not statistically significant.

(ix) In future work, we are aiming to obtain $\alpha'(^{12}\mathrm{CO})$ measurements for more GMCs in M31 for which we also have H II region abundances, so that the correlation between the two factors can be investigated further. We will also investigate the chemical abundance throughout the M31 disc further through analysis of log(N/O).

ACKNOWLEDGEMENTS

The authors thank the anonymous referee for helpful comments. Observations reported here were obtained at the MMT Observatory, a joint facility of the Smithsonian Institution and the University of Arizona. CK acknowledges funding from the UK Science and Technology Facility Council (STFC) through grants ST/Y001443/1.

DATA AVAILABILITY

H II region spectra can be shared upon reasonable request.

REFERENCES

Arnaboldi M. et al., 2022, A&A, 666, a109
Arnett D., Chevalier R., 1996, Phys. Today, 49, 68
Arp H., 1964, ApJ, 139, 1045
Azimlu M., Marciniak R., Barmby a., 2011, AJ, 142, 139
Baldwin J. A., Phillips M. M., Terlevich R., 1981, PASP, 93, 5
Balser D. S., Rood R. T., Bania T. M., Anderson L. D., 2011, ApJ, 738, 27
Belfiore F. et al., 2017, MNRAS, 469, 151
Bhattacharya S. et al., 2019, A&A, 631, A56
Bhattacharya S. et al., 2022, MNRAS, 517, 2343
Block D. L. et al., 2006, Nature, 443, 832
Bolatto A. D., Wolfire M., Leroy A. K., 2013, ARA&A, 51, 207
Bothwell M., Maiolino R., Cicone C., Peng Y., Wagg J., 2016, A&A, 595, A48
Braun R., 1991, ApJ, 372, 54
Bresolin F., Stasińska G., Vílchez J. M., Simon J. D., Rosolowsky E., 2010, MNRAS, 404, 1679

Cardelli J. A., Clayton G. C., Mathis J. S., 1989, ApJ, 345, 245
Clayton D., 1983, Principles of Stellar Evolution and Nucleosynthesis, Univ. Chicago Press, Chicago
Davidge T. J., McConnachie A. W., Fardal M. A., Fliri J., Valls-Gabaud D., Chapman S. C., Lewis G. F., Rich R. M., 2012, ApJ, 751, 74
de Avillez M. A., Low M.-M. M., 2002, ApJ, 581, 1047
Devereux N. A., Price R., Wells L. A., Duric N., 1994, AJ, 108, 1667
Dierickx M., Blecha L., Loeb A., 2014, ApJ, 788, L38
Earl N. et al., 2024, astropy/specutils: v1.16.0, Zenodo, doi: 10.5281/zenodo.13829659
Esteban C., García-Rojas J., 2018, MNRAS, 478, 2315
Fabricant D. et al., 2005, PASP, 117, 1411
Forbrich J., Lada C., Viaene S., Petitpas G., 2020, ApJ, 890, 42
Gordon K. D. et al., 2006, ApJ, 638, L87
Grasha K. et al., 2022, ApJ, 929, 118
Groves B. et al., 2023, MNRAS, 520, 4902
Haas M., Lemke D., Stickel M., Hippelein H., Kunkel M., Herbstmeier U., Mattila K., 1998, A&A, 338, L33
Habing H. J. et al., 1984, ApJ, 278, L59
Haud U., 1981, Ap&SS, 76, 477
Henry R. B. C., Worthey G., 1999, PASP, 111, 919
Ho I.-T., 2019, MNRAS, 485, 3569
Ho I.-T. et al., 2017, ApJ, 846, 39
Ho I. T. et al., 2018, A&A, 618, A64
Jin Y., Sutherland R., Kewley L. J., Nicholls D. C., 2023, ApJ, 958, 179
Kauffmann G. et al., 2003, MNRAS, 346, 1055
Kewley L. J., Dopita M. A., 2002, ApJS, 142, 35
Kewley L. J., Ellison S. L., 2008, ApJ, 681, 1183
Kewley L. J., Dopita M. A., Sutherland R. S., Heisler C. A., Trevena J., 2001, ApJ, 556, 121
Kewley L. J., Nicholls D. C., Sutherland R. S., 2019, ARA&A, 57, 511
Khoperskov S., Sivkova E., Saburova A., Vasiliev E., Shustov B., Minchev I., Walcher C. J., 2023, A&A, 671, A56
Kirk J. M. et al., 2015, ApJ, 798, 58
Kniazev A. Y., Pustilnik S. A., Zucker D. B., 2008, MNRAS, 384, 1045
Kobayashi C., Karakas A. I., Lugaro M., 2020, ApJ, 900, 179
Kobayashi C., Bhattacharya S., Arnaboldi M., Gerhard O., 2023, ApJ, 956, L14
Kobulnicky H. A., Kewley L. J., 2004, ApJ, 617, 240
Kreckel K. et al., 2019, ApJ, 887, 80
Kreckel K. et al., 2020, MNRAS, 499, 193
Leitherer C. et al., 1999, ApJS, 123, 3
Lequeux J., Peimbert M., Rayo J. F., Serrano A., Torres-Peimbert S., 1979, A&A, 80, 155
Lewis A. R. et al., 2015, ApJ, 805, 183
Maiolino R., Mannucci F., 2019, A&AR, 27, 3
Mannucci F., Cresci G., Maiolino R., Marconi A., Gnerucci A., 2010, MNRAS, 408, 2115
Marino R. A. et al., 2013, A&A, 559, A114
Matteucci F., Franco J., Francois P., Treyer M.-A., 1989, RMxAA, 18, 145
Momcheva I. G., Lee J. C., Ly C., Salim S., Dale D. A., Ouchi M., Finn R., Ono Y., 2013, AJ, 145, 47
Nagao T., Maiolino R., Marconi A., 2006, A&A, 459, 85
Nieten C., Neininger N., Guélin M., Ungerechts H., Lucas R., Berkhuijsen E. M., Beck R., Wielebinski R., 2006, A&A, 453, 459
Osterbrock D., Ferland G., 2006, Astrophysics Of Gas Nebulae and Active Galactic Nuclei, University Science Books, Virginia
Pagel B. E. J., Edmunds M. G., Blackwell D. E., Chun M. S., Smith G., 1979, MNRAS, 189, 95
Pelupessy F. I., Papadopoulos P. P., 2009, ApJ, 707, 954
Pettini M., Pagel B. E. J., 2004, MNRAS, 348, L59
Pilyugin L. S., Grebel E. K., 2016, MNRAS, 457, 3678 PG16
Pilyugin L. S., Thuan T. X., 2005, ApJ, 631, 231
Pilyugin L. S., Vílchez J. M., Thuan T. X., 2010, ApJ, 720, 1738
Roy J. R., Kunth D., 1995, A&A, 294, 432
Sánchez-Menguiano. L. et al., 2016, A&A, 587, A70
Sanders N. E., Caldwell N., McDowell J., Harding P., 2012, ApJ, 758, 133 S12
Shetty R., Glover S. C., Dullemond C. P., Ostriker E. C., Harris A. I., Klessen R. S., 2011, MNRAS, 415, 3253
Simien F., Pellet A., Monnet G., 1979, A&A, 72, 12
Stanek K. Z., Garnavich P. M., 1998, ApJ, 503, L131
Stasińska G. et al., 2008, MNRAS, 391, L29
Storey P. J., Zeippen C. J., 2000, MNRAS, 312, 813
Tinsley B. M., 1980, Fund. Cosmic Phys., 5, 287
Viaene S., Forbrich J., Lada C. J., Petitpas G., Faesi C., 2021, ApJ, 912, 68
Vincenzo F., Kobayashi C., 2018, MNRAS, 478, 155
Vincenzo F., Kobayashi C., 2020, MNRAS, 496, 80
Wenger T. V., Balser D. S., Anderson L. D., Bania T. M., 2019, ApJ, 887, 114
Williams T. G. et al., 2022, MNRAS, 509, 1303
Zaritsky D., Kennicutt Robert C. J., Huchra J. P., 1994, ApJ, 420, 87 Z94

SUPPORTING INFORMATION

Supplementary data are available at *MNRAS* online.

suppl_data

Please note: Oxford University Press is not responsible for the content or functionality of any supporting materials supplied by the authors. Any queries (other than missing material) should be directed to the corresponding author for the article.

APPENDIX A: EMISSION LINE PROFILES

As an example, we show emission line profiles for the strong lines measured (see Section 3.1) to calculate O and N abundances (see Section 3.4) for two spectra from M31 H II regions in our sample in Fig. A1. One spectrum from the top 2 per cent highest signal-to-noise spectra in our sample, corresponding to row 7 in Tables 1 and 2, and one spectrum from the bottom 30 per cent lowest signal-to-noise spectra in our sample, corresponding to row 6 in Tables 1 and 2. The respective Gaussian fits to each line profile are additionally shown.

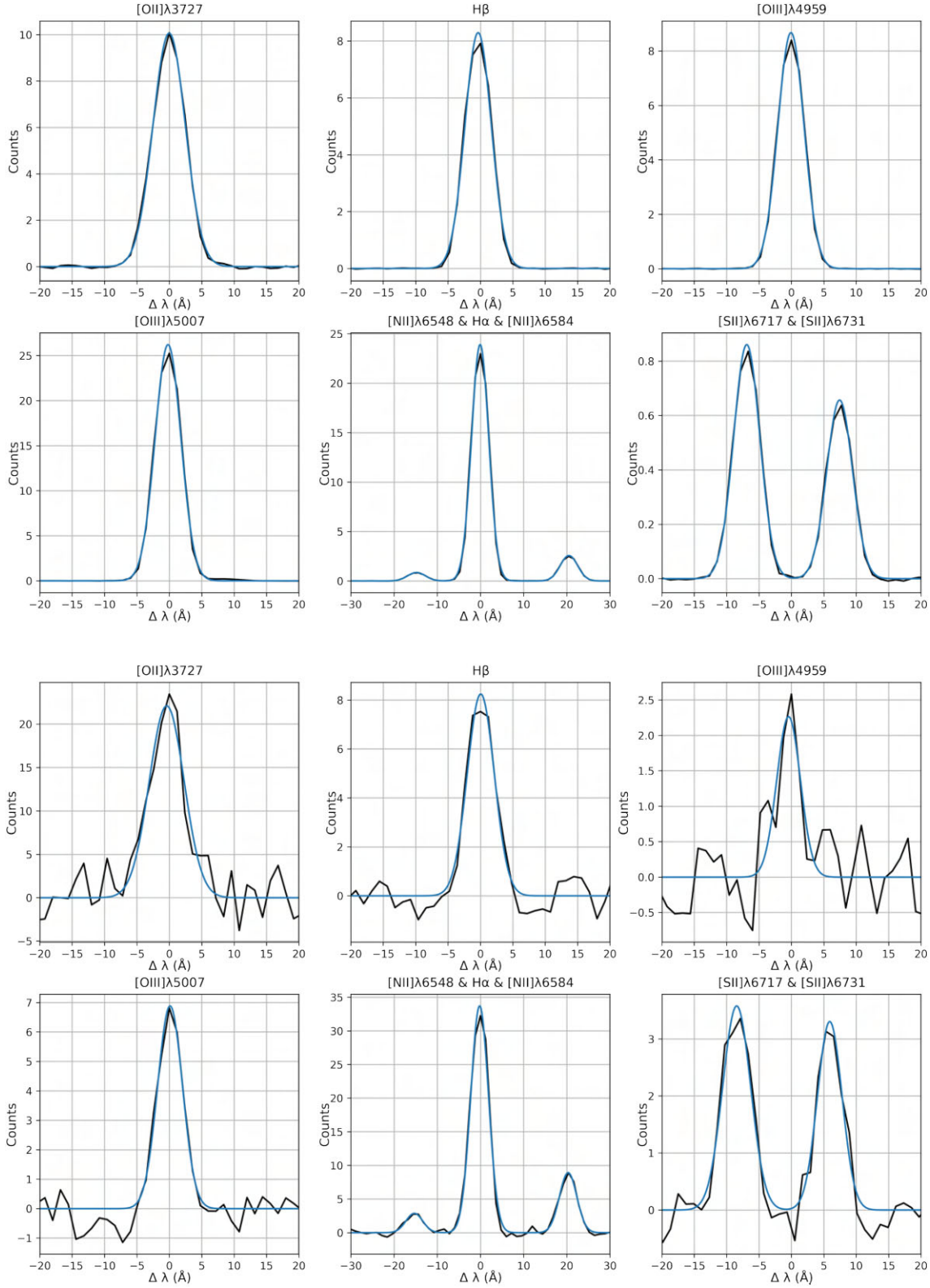

Figure A1. Emission line profiles for the strong lines measured in two example spectra. *Top*: spectrum in the top 2 per cent signal-to-noise (row 7 from the data tables). *Bottom*: spectrum in the bottom 30 per cent signal-to-noise (row 6 from the data tables). On the *x*-axis, 0 represents the rest-wavelength of the lines. In the case the line profile of Hα and the [N II] doublet, we centre the wavelength-axis on the midpoint of Hα. For the [S II] doublet, we centre the wavelength-axis on the mid-point between the rest wavelengths of both lines.

This paper has been typeset from a TEX/LATEX file prepared by the author.